Nat. Hazards Earth Syst. Sci., 24, 225–243, 2024
https://doi.org/10.5194/nhess-24-225-2024

Natural Hazards and Earth System Sciences
Open Access
EGU

Using integrated hydrological–hydraulic modelling and global data sources to analyse the February 2023 floods in the Umbeluzi Catchment (Mozambique)

Luis Cea, Manuel Álvarez, and Jerónimo Puertas

Water and Environmental Engineering Group, Center for Technological Innovation in Construction and Civil Engineering (CITEEC), Campus de Elviña, Universidade da Coruña, 15071 A Coruña, Spain

Correspondence: Luis Cea (luis.cea@udc.es)

Received: 16 May 2023 – Discussion started: 15 June 2023
Revised: 10 November 2023 – Accepted: 29 November 2023 – Published: 30 January 2024

Abstract. On 9–13 February 2023 an intense flood event took place in the province of Maputo (Mozambique), resulting in severe damage to agricultural lands and transport infrastructure and with serious consequences for the population. In the district of Boane, located a few kilometres downstream of the Pequenos Libombos dam, the flood destroyed many food crops as well as two bridges linking the district to Maputo, thus affecting the food security of the population. These events are quite frequent in this region, making the delineation of improved flood hazard maps and the development of new flood risk management plans necessary. We reproduce this flood event with a high-resolution integrated hydrologic–hydraulic model fed with freely available global data sources, using a methodology that can be easily reproduced in other data-scarce regions. The model results are validated with observed estimations of the inflow to the Pequenos Libombos reservoir, with water marks left by the flood in the district of Boane, and with a Sentinel-1 image taken during the recession of the flood. We analyse the effect of the Pequenos Libombos reservoir on the flood hazard, which was subject to debate among the affected population and in the media. The results obtained show that integrated hydrologic–hydraulic models based on two-dimensional shallow-water equations, combined with global databases, are currently able to reasonably reproduce the extent and peak discharge of extreme flood events in data-scarce basins and are therefore very useful tools for the development of flood management plans in these regions.

1 Introduction

As with many other African countries, Mozambique is highly exposed to the impact of floods and to the effects of climate change (Revilla-Romero et al., 2014; World Bank, 2019). This is mainly due to the high vulnerability of its communities, combined with the extreme rainfalls produced by the tropical storms and cyclones that occur on its coastline on average every 2 years (WMO, 2019). Moreover, Mozambique's population is forecast to grow from 30 to 65 million over the next 30 years and will concentrate near rivers, lakes, and the coastline, thus increasing the exposure of these populations to the impact of floods. In light of this, Mozambique has made significant efforts in recent years to put flood risk evaluation and mitigation measures in place.

The heavy rains that occurred in southern Mozambique between 6 and 15 February 2023 resulted in local rainfall depths of 350 mm, causing widespread flooding and considerable damage, especially in the city of Maputo and its neighbourhood. According to the data provided by the National Institute for Disaster Risk Reduction and Management (INGD), as of 17 February, 43 426 people have been affected by the floods, with 16 600 people displaced and 10 deaths (OCHA, 2023). The district of Boane, located downstream of the Pequenos Libombos (PL) dam and crossed by the waters of the Umbeluzi River and its tributary Movene, was the most affected part of the province. With a very flat topography, many neighbourhoods in this area were wholly inundated and isolated, given that road traffic was interrupted on the EN2 National Road that connects the city of Matola to the village of Boane. The Mazambabine and Boane bridges

were submerged, and the drinking water treatment plant was disrupted, resulting in significant cuts in water supply to the population. Upstream of the PL dam, the steel bridge over the Umbeluzi River linking the Michangulene and Mafavuka settlements was swept away, and the bridge over the Calichane River on the EN3 National Road connecting Mozambique to Eswatini was partially destroyed.

The PL dam is located in the district of Namaacha, in the province of Maputo, and is the main water infrastructure located on the Umbeluzi River within the territory of Mozambique. It was built between 1981 and 1987, and its main purpose is the supply of water to the cities of Maputo, Matola, and Boane, as well as the irrigation of agricultural lands. The storage capacity of the reservoir is 385 hm^3, corresponding to a maximum operation level or normal pool level (NPL) of 47.00 m. The design flood level, or maximum pool level (MPL), is at 49.55 m, just 0.5 m below the crest of the dam. The spillways of the dam are controlled by movable gates and have their crest at an elevation of 24.00 m, the reservoir's volume at that level being 8 hm^3. Thus, the reservoir's outlet discharge can be controlled for almost its full range of capacity.

During the first 8 d of February, the reservoir remained at an average level of 45.56 m, corresponding to a storage volume of 331.2 hm^3 and 86.1 % of its NPL capacity. During the following 2 d, an intense rainfall event within the basin led to a maximum daily inflow discharge of 3848 $m^3\,s^{-1}$. The reservoir level reached 48.50 m, corresponding to 451.6 hm^3 and 117.3 % of its NPL capacity. In this critical situation, and in order to guarantee the structural safety of the dam, it was necessary to release water at the spillways' maximum capacity (around 2870 $m^3\,s^{-1}$). The situation remained practically unchanged until 10 February, when the reservoir level dropped slightly to 48.20 m.

In this study we reproduced the flood event that took place on 9–13 February 2023 in the Umbeluzi Basin using Iber+ software, a GPU-enhanced high-resolution integrated hydrologic–hydraulic model based on two-dimensional shallow-water equations (Bladé et al., 2014; Cea and Bladé, 2015; García-Feal et al., 2018). This kind of modelling approach has become increasingly popular in recent years due to the development of efficient numerical solvers that implement different GPU or CPU parallelisation techniques, making it possible to solve the two-dimensional shallow-water equations in a whole catchment using grids of several millions of elements (Caviedes-Voullième et al., 2023; García-Feal et al., 2018; Morales-Hernández et al., 2021; Noh et al., 2018; Sanders and Schubert, 2019; Sharifian et al., 2023; Xia et al., 2019).

The model parameters were defined from standard non-calibrated values, and all input data were obtained from global data sources that are freely available worldwide, making the methodology reproducible anywhere. We evaluated the ability of this type of model to reproduce flood events in data-scarce regions, where it is necessary to rely on global databases, and where detailed observed data are not available for the calibration of model parameters. To this end, the model results were validated with the following: (1) inflows to the PL reservoir during the event, provided by the regional water administration ARA-Sul; (2) maximum water depths, estimated from the identification of water marks left by the flood at different points in the district of Boane; and (3) the extent of the water, estimated from a Sentinel-1 image taken during the recession of the flood. Once the model was validated, the effect that the management of the PL reservoir had on the spatial extent of the inundation and on the maximum water depths reached in the surroundings of Maputo was analysed. For this purpose, three modelling scenarios were reproduced numerically: MS1 represents the actual management of the PL reservoir that took place during the storm event, MS2 reproduces what would have happened in the absence of the PL reservoir, and MS3 predicts what would have happened if the PL reservoir had been able to retain the total inflow hydrograph that arrived there during the storm event.

The results obtained show that integrated hydrologic–hydraulic models based on two-dimensional shallow-water equations, combined with global databases, are currently able to reproduce the extent and peak discharge of extreme flood events in data-scarce basins and are therefore very useful tools for the development of flood management plans in these regions. The accuracy of the water depth predictions might however be limited in certain regions by the spatial resolution and accuracy of the global topographic data currently available. In the case of the February 2023 floods in the Umbeluzi Catchment, it can be claimed that the management of the PL reservoir contributed to the reduction of the flood hazard in Boane, although the effect was relatively small due to the limited flood control capacity of the reservoir and the high magnitude of the flood. In the absence of the dam, the impact of the flood would have been far greater.

2 Case study: the Umbeluzi Catchment

The Umbeluzi Catchment is one of the largest catchments in southern Mozambique. It has a total surface of 5461 km^2, distributed between Mozambique (40.7 %), Eswatini (57.6 %), and South Africa (1.7 %). The Umbeluzi River originates in the foothills of the Malolotja Nature Reserve, at an altitude of 1393 m. After extending for about 290 km in a west–east direction, it flows into the Indian Ocean. The outlet of the catchment considered in this study (Fig. 1) is located 7.2 km upstream of the junction of the Umbeluzi, Matola, and Tembe rivers (coordinates of UTM zone 36S: 7 119 978 m N, 443 993 m E) in the estuary of Espírito Santo.

The average elevation of the Umbeluzi Basin is 346 m a.m.s.l., ranging from 0 to 1828 m, with an average slope of 9.9 %. The central and eastern parts of the basin, which occupy 73.7 % of its surface, have a flat or moderate

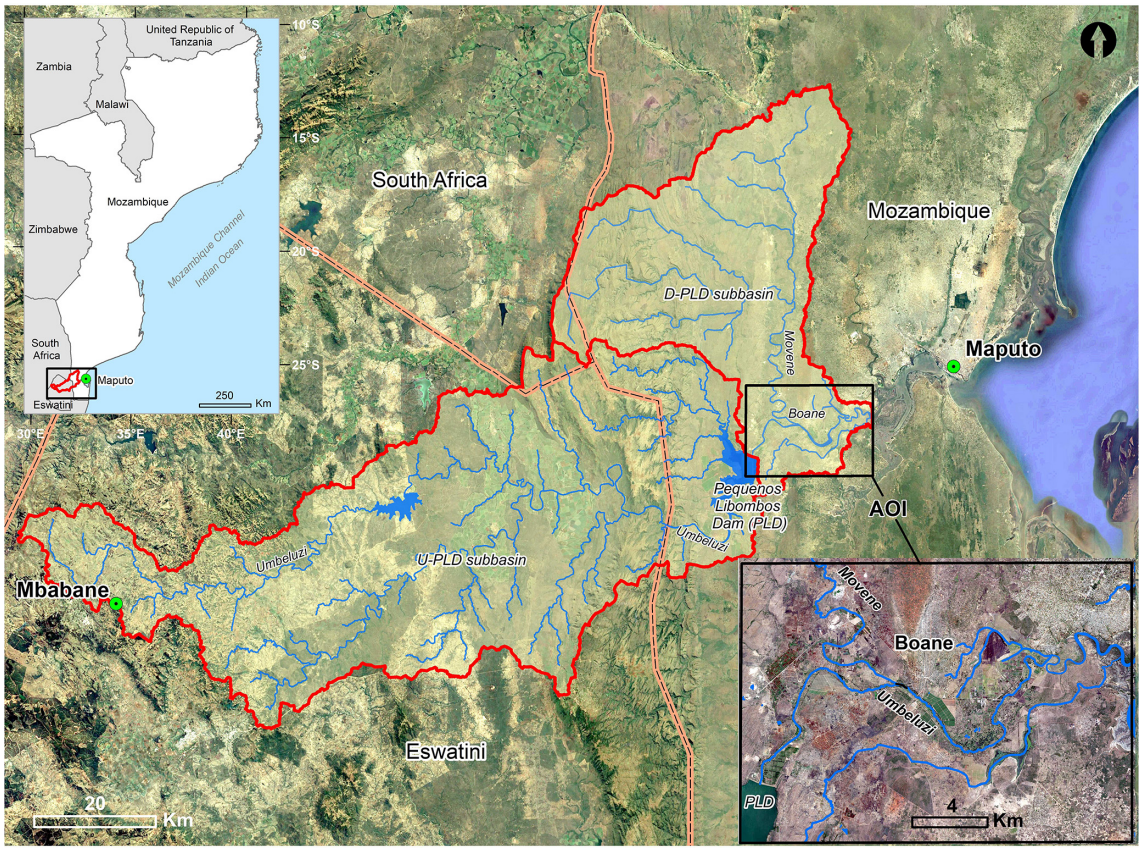

Figure 1. Location map of the Umbeluzi Catchment, divided into two subbasins, U-PLD and D-PLD, located upstream and downstream of the PL dam respectively, and definition of the area of interest (AOI) for this study. Background image: © Google Earth version 7.3.6.9345, http://www.earth.google.com (last access: 13 April 2023).

slope (less than 12 %). These parts of the basin are divided by the Pequenos Libombos mountain range, which runs in a north–south direction along the border of Mozambique with Eswatini and South Africa. In this area the relief is undulating or very steep, with slopes over 75 % and reaching maximum slope values close to 160 %.

The average annual precipitation in the entire Umbeluzi Basin during the 1981–2010 period, estimated from the Climate Hazards Group InfraRed Precipitation with Station data (CHIRPS) daily data source (Funk et al., 2015), was 744 mm. The spatial distribution of rainfall varies from 600 mm in the flat areas of the lower part of the basin to 1300 mm in the more mountainous headwater areas. The wet period is from October to March and accounts for 84 % of total annual precipitation.

For the purpose of this study, the Umbeluzi catchment was split into two complementary regions, as shown in Fig. 1. The first region includes the catchment located upstream of the PL dam, while the second region includes the catchment located downstream of the PL dam. In what follows, we refer to these two regions as the upstream Pequenos Libombos dam (U-PLD) and the downstream Pequenos Libombos dam (D-PLD).

The part of the basin located downstream of the PL dam (D-PLD in Fig. 1) is one of the most flood-prone regions in the Maputo province. With an area of 1723 km^2, this subbasin has been impacted by intense floods in the years 1966, 1972, 1977, 1984, and 2000. Moreover, during the hydrological years 2016 and 2020, the tropical cyclones Dineo, Chalane, Eloise, and Guambe–Eloise caused significant flooding. Historical records from a hydrometric station located in Boane, prior to the construction of the PL dam, indicate that the 1984 flood was the largest of all registered floods, with a maximum discharge of the order of 7250 $m^3 s^{-1}$ (Lacamurima, 2003).

The analysis of flood hazard in this study focuses on an area of interest (AOI) of 313 km^2 distributed over the districts of Boane (83 %) and Naamacha (17 %) (Fig. 1). This is a very vulnerable area in terms of flood damage since it is located just a few kilometres downstream of the PL dam, thus receiving the outflow discharge from the reservoir, as well as the surface runoff generated by rainfall falling in the

D-PLD subbasin, the major contribution of which is from the Movene River basin.

3 Methodology

3.1 Global data sources

The various global data sources used in this work are listed in Table 1, which also includes their spatial resolution and the URL where they can be retrieved without cost. In what follows, the most relevant features of each data set for hydrological modelling purposes are described.

3.1.1 Digital elevation model

The topography of the whole Umbeluzi Catchment (Fig. 2) was obtained from the Copernicus GLO-30 digital elevation model (DEM), which has a spatial resolution of 1 arcsec (roughly 30 m). This is the highest-resolution global DEM generated and is provided free of charge by the European Space Agency (ESA). It was obtained by the ESA after processing the data from the TanDEM-X mission, which took place between 2011 and 2015 (Krieger et al., 2013; Zink et al., 2021), covering the whole Earth with a spatial resolution of 12 m. The ESA also provides a DEM obtained from TanDEM-X at a spatial resolution of 0.4 arcsec (EEA-10) but only covering European states. There is also a commercial version of TanDEM-X with a spatial resolution of 12 m (WorldDEM™) edited by Airbus Defence and Space (Bayburt et al., 2017), but it is not available free of charge.

Several recent studies in various regions of the world have concluded that Copernicus GLO-30 is the DEM with the best overall performance for hydrological modelling purposes that is currently available for free (Cea et al., 2022; Garrote, 2022; Guth and Geoffroy, 2021; Maresova et al., 2021), producing a better representation of the terrain for hydrological and hydraulic computations than other commonly used 1 arcsec DEMs, such as ALOS, ASTER, NASADEM, and SRTM v3.

3.1.2 Rainfall

There are currently several freely available data sets providing global rainfall estimates that can be used for a variety of hydrological studies. In the case of flood modelling, the products derived from the Global Precipitation Measurement (GPM) satellite constellation of the National Aeronautics and Space Administration (NASA) (Huffman et al., 2020) are of particular interest due to their low latency and high spatial and temporal resolution. The Integrated Multi-satellitE Retrievals for GPM (GPM-IMERG) has been providing precipitation estimates since March 2014 within the 60° N–S latitude band, at maximum spatial and temporal resolutions of 0.1° (roughly 10 km) and 30 min, with latencies of 4 h (Early run), 14 h (Late run), and 3–4 months (Final run). When modelling relatively short and intense rainfall events, having rainfall estimates every 30 min is a clear advantage over other global products that work at lower temporal resolutions, as for instance CHIRPS, which provides estimates with a resolution of 1 d. Pradhan et al. (2022) provide a review of different GPM-IMERG validation studies at various locations around the globe. Other studies, such as Saouabe et al. (2020), Liu et al. (2020), or Tapiador et al. (2021), among others, also evaluated the accuracy of GPM-IMERG compared to observed rainfall in different parts of the world, concluding that the use of GPM contributes extraordinarily to improving the monitoring of extreme rainfall events when ground-based precipitation data are not available. In the case of Africa, a recent review by Gosset et al. (2023) about the role of satellite observations in monitoring pluvial and fluvial floods highlighted that major recent flood events in Africa have been well depicted by satellite observations, illustrating the feasibility of satellite monitoring for better surveillance of the food risk in this region.

In the present study we have used the GPM-IMERG Late run data set, with 0.1° and 30 min spatial and temporal resolutions, to represent the rainfall fields during the storm event that took place on 7–14 February 2023 over the Umbeluzi Catchment. The Umbeluzi Basin is covered by 66 rainfall pixels. The rainfall estimates between 6 February 2023 at 00:00 UTC and 15 February 2023 at 00:00 UTC (432 files) were used as rainfall input in the numerical model. Figure 3 shows the spatial distribution of rainfall depth over the catchment during the simulation period, as well as the basin-averaged rainfall depth–duration curve. Most of the rainfall (around 170 mm) fell on 8–9 February, while a second burst of about 50 mm fell within 10 h on 12 February. The total basin-averaged rainfall depth during the event was around 240 mm.

The analysis of the spatial pattern of the rainfall over the basin shows that there was a cluster with cumulative rainfall depths above 300 mm covering an area of 1084 km^2. Within this core, a cell with a local maximum of 356 mm was located 12 km west of the PL dam. The spatial distribution of the rainfall event also shows that, towards the upper part of the basin, the cumulative rainfall depth decreases progressively until it reaches a local minimum of 79 mm. This distribution pattern, with maxima close to the outlet of the U-PLD subbasin, contributed to reducing the response time of the basin, thus increasing the peak discharges flowing into the PL dam.

3.1.3 Land cover

The propagation of overland flow over the hillslopes and along the river network was computed with the Iber software, which solves the two-dimensional shallow-water equations, using a roughness coefficient that depends on the land cover to characterise the bed friction between the terrain and the water. Hence, land cover maps are needed in order to es-

Table 1. Data sets used in the numerical model.

Variable	Data set	Resolution	Source
DEM	Copernicus GLO-30	30 m	https://panda.copernicus.eu/web/cds-catalogue (last access: 1 March 2022)
Rainfall	GPM IMERG Final Precipitation L3	10 km, 30 min	https://disc.gsfc.nasa.gov (last access: 1 March 2022)
Land cover	ESA WorldCover 10m 2021 v200	10 m	http://due.esrin.esa.int/page_globcover.php (last access: 1 March 2022)
Infiltration	GCN250	250 m	https://doi.org/10.6084/m9.figshare.7756202.v1

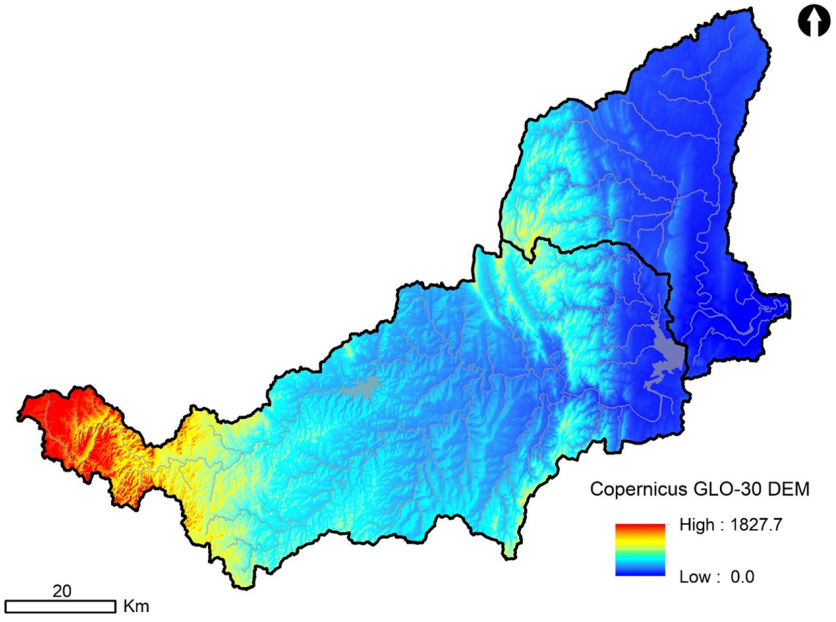

Figure 2. Topography of the Umbeluzi Catchment obtained from the Copernicus GLO-30 DEM.

timate the spatial distribution of the roughness coefficient across the whole catchment.

From the various land cover maps that are currently available at the global scale, we have used WorldCover 10m 2021, recently released by the ESA. This product was generated within the framework of the ESA WorldCover project, itself part of the 5th Earth Observation Envelope Programme (EOEP-5). It provides a global land cover classification for 2021 at a spatial resolution of 10 m, derived from Sentinel-1 and Sentinel-2 data, including 11 land cover classes. It is currently the most recent and highest-resolution global land cover product available free of charge. The land cover distribution across the Umbeluzi Catchment is shown in Fig. 4. Trees and grassland are the two predominant land uses, each making up around 38 % of the basin. Cropland and shrubland cover 12 % and 10 % of the catchment surface respectively, while the other four land uses present in the basin (built-up, sparse vegetation, permanent water bodies, and herbaceous wetlands) represent only 2 % of the surface.

3.1.4 Infiltration

The infiltration capacity of the terrain can be characterised using different empirical formulations (Singh, 2017). In the case of flood modelling, one of the methods most commonly used to estimate the potential infiltration of the soil is the Natural Resources Conservation Service (formerly Soil Conservation Service) curve number (SCS-CN). In the absence of detailed field data, it has the advantage of using a single parameter (CN) that has been extensively tabulated as a function of the hydrological soil group, the land cover, and the terrain slope (Singh, 2017). Thus, it is especially suitable in data-scarce regions, where the lack of field data that could be used for calibration hinders the application of other (also well-known) formulations such as those of Green-Ampt and Horton.

In order to estimate the potential infiltration in the numerical model, we have used the data set GCN250 (Jaafar et al., 2019), which includes a global estimation of CN for the whole Earth with a spatial resolution of 250 m.

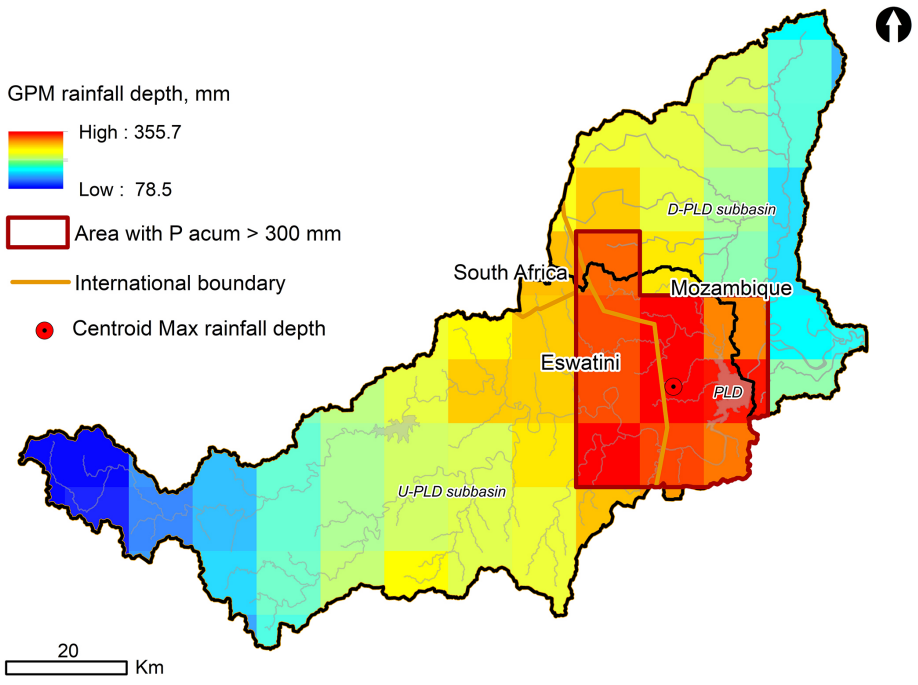

Figure 3. Spatial distribution of rainfall depth in the Umbeluzi Catchment from 7–14 February 2023, obtained from the GPM-IMERG database, and time series of basin-averaged rainfall depth in the U-PLD and D-PLD subbasins.

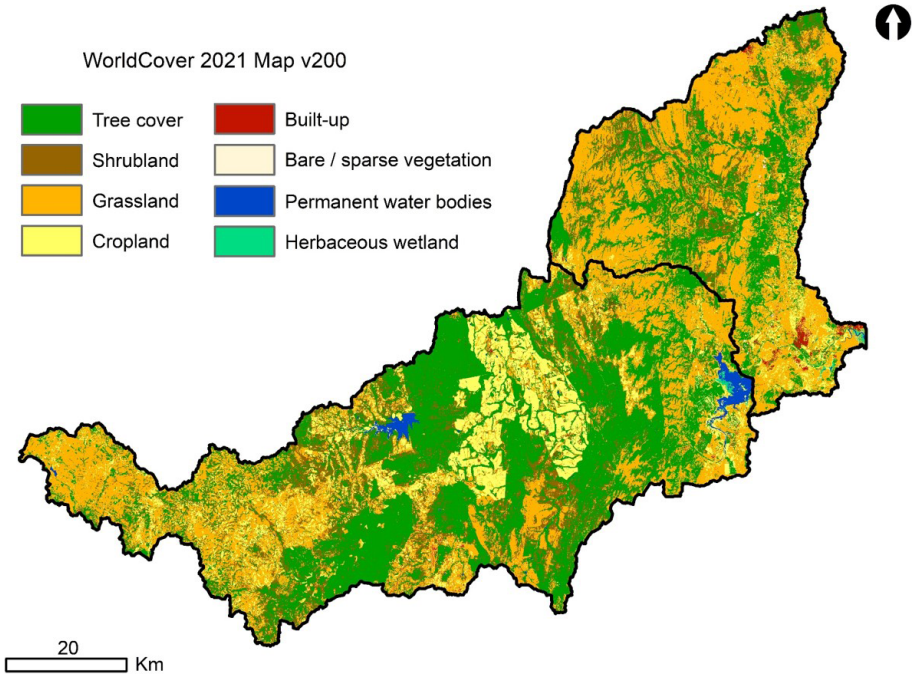

Figure 4. Land cover in the Umbeluzi Catchment obtained from the ESA WorldCover 10m 2021 v200.

The CN values provided by this data set were derived by considering global maps of hydrological soil groups (HYSOGs250m) and land cover (ESA CCI Land Cover project). The HYSOGs250m data set (Ross et al., 2018) was specially derived in order to support SCS-CN runoff modelling at global scales using soil data from the FAO Harmonized World Soil Database.

The data set includes CN estimates for average, wet, and dry antecedent moisture content (AMC) of the soil, computed according to the SCS-CN methodology. In order to model the flood of 9–13 February 2023, we considered wet AMC conditions, since the 5 d antecedent rainfall depth in the basin was slightly greater than 50 mm.

Figure 5 shows the spatial distribution of CN within the Umbeluzi Basin for wet AMC soil conditions, which varies between 85 and 98 in the hillslopes and floodplains, with a basin-averaged value of 91.

3.2 Numerical model

The software used in this study (Iber) solves the two-dimensional shallow-water equations (2D-SWE) in the whole catchment with an integrated hydrological–hydraulic modelling approach. Iber implements rainfall and infiltration processes within the shallow-water equations, allowing the simulation of rainfall–runoff transformation and river inundation processes simultaneously (Cea and Bladé, 2015). The model implements an unstructured finite-volume solver for the 2D-SWE, allowing the user to adapt the mesh to the basin morphology and to define a variable mesh size in different regions of the study area. This kind of modelling approach has been used in previous studies, in which its suitability for modelling rainfall–runoff transformation and overland flow propagation at the catchment scale during intense flood events has been shown (Cea et al., 2022; García-Alén et al., 2022; Sanz-Ramos et al., 2021; Moral-Erencia et al., 2021; Xia et al., 2019). Moreover, the application and validation of Iber to event-based hydrological computations at different spatial scales have been presented in several previous studies (Cea et al., 2010; Fraga et al., 2019; García-Alén et al., 2023; Sanz-Ramos et al., 2018, 2022; Tamagnone et al., 2020; Uber et al., 2021). The high-performance computing (HPC) implementation of the Iber software (Iber+) is especially suitable for integrated hydrological–hydraulic modelling applications because it can achieve speed-ups of 2 orders of magnitude with respect to the standard sequential implementation (García-Feal et al., 2018).

A different model was built for the U-PLD and D-PLD subbasins, as shown in Fig. 6. The U-PLD model was used to compute the hydrograph entering the PL reservoir and to validate the modelling approach by comparing the computed hydrograph with the observed one. The D-PLD model was used to compute the flood hazard in the district of Boane, considering in an integrated way the reservoir's outlet hydrograph during the event and the overland flow generated by the rainfall falling directly in the D-PLD subbasin.

In both models the spatial domain was discretised with an unstructured mesh of triangular elements, adapted to the basin's morphology, introducing an explicit representation of the river network and using different element sizes in the hillslopes and in the river streams. To this end, the river network was defined from the DEM, considering first a minimum contributing drainage area (CDA) of 1 km^2, and then keeping only the streams with a Strahler order larger than 5. Once the stream network was delineated in this way, the width of the main channel was estimated to 100 m, based on visual inspection of orthophotos. The size of the mesh elements ranged from 25 m in the main river reaches to 80 m in the hillslopes. It should be noted that the distinction between the river network and hillslopes obtained in this way is only relevant in order to define the mesh size and the bed roughness coefficient and does not have any implications in terms of the type of equations or the numerical schemes implemented to compute the propagation of runoff, since the same numerical solver is applied to the whole spatial domain. This type of discretisation of the spatial domain has already been applied in previous studies with good results (Cea et al., 2022; Komi et al., 2017; Uber et al., 2021).

When applying this procedure to the Umbeluzi Catchment, the river networks obtained have total lengths of 530 and 350 km in the U-PLD and D-PLD models respectively (Fig. 6). Those streams were discretised with 120 000 elements in the U-PLD model and 83 000 elements in the D-PLD model. Regarding the hillslopes, in the U-PLD model they covered a surface of 3681 km^2 and were discretised with over 1.4 million elements, while the D-PLD model had around 1.1 million elements to cover a hillslope surface of 1697 km^2. Considering both models and the whole Umbeluzi Catchment, the total modelled surface was 5461 km^2, and the total number of elements was approximately 2.6 million.

The hydrodynamic equations solved by the Iber software can be expressed as

$$\frac{\partial h}{\partial t} + \frac{\partial q_x}{\partial x} + \frac{\partial q_y}{\partial y} = R - i, \tag{1}$$

$$\frac{\partial q_x}{\partial t} + \frac{\partial}{\partial x}\left(\frac{q_x^2}{h} + g\frac{h^2}{2}\right) + \frac{\partial}{\partial y}\left(\frac{q_x q_y}{h}\right) = -gh\frac{\partial z_b}{\partial x} - g\frac{n^2}{h^{7/3}}|q|q_x, \tag{2}$$

$$\frac{\partial q_y}{\partial t} + \frac{\partial}{\partial x}\left(\frac{q_x q_y}{h}\right) + \frac{\partial}{\partial y}\left(\frac{q_y^2}{h} + g\frac{h^2}{2}\right) = -gh\frac{\partial z_b}{\partial y} - g\frac{n^2}{h^{7/3}}|q|q_y, \tag{3}$$

where h is the water depth; q_x, q_y, and $|q|$ are the two components of the unit discharge and its modulus; z_b is the bed elevation; n is the Manning coefficient; g is the gravity acceleration; R is the rainfall intensity; and i is the infiltration rate. All the input data and parameters (rainfall fields, infiltration parameters, and Manning coefficient) can vary in space.

As noted in Sect. 3.1.4, the soil infiltration capacity was modelled using the SCS-CN method. The spatial distribution of CN obtained from the GCN250 data set (Jaafar et al., 2019) was used to assign the CN in the hillslopes and floodplains, but its spatial resolution is not high enough to capture

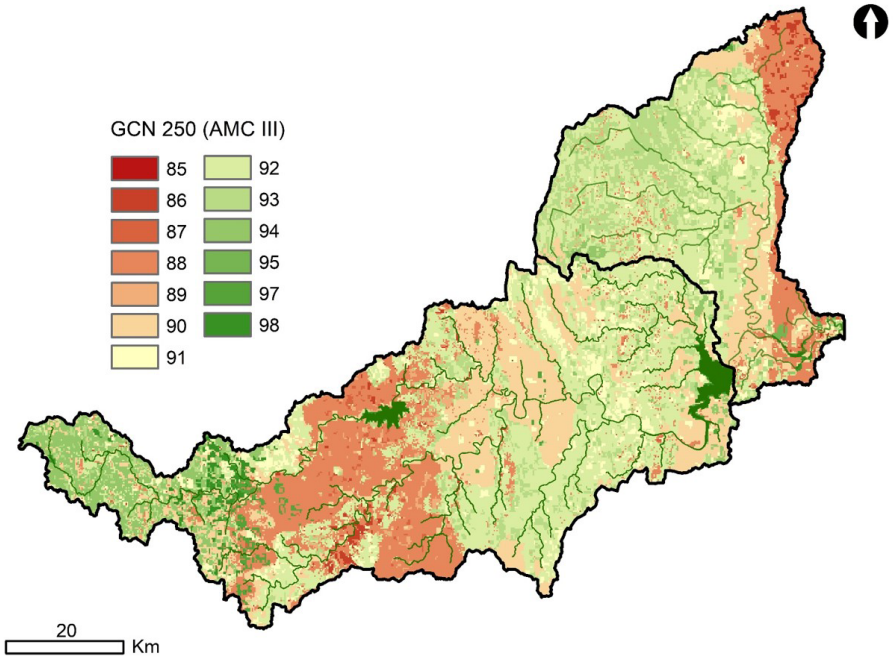

Figure 5. Spatial distribution of CN for wet AMC conditions in the Umbeluzi Catchment, obtained from GCN250 (Jaafar et al., 2019).

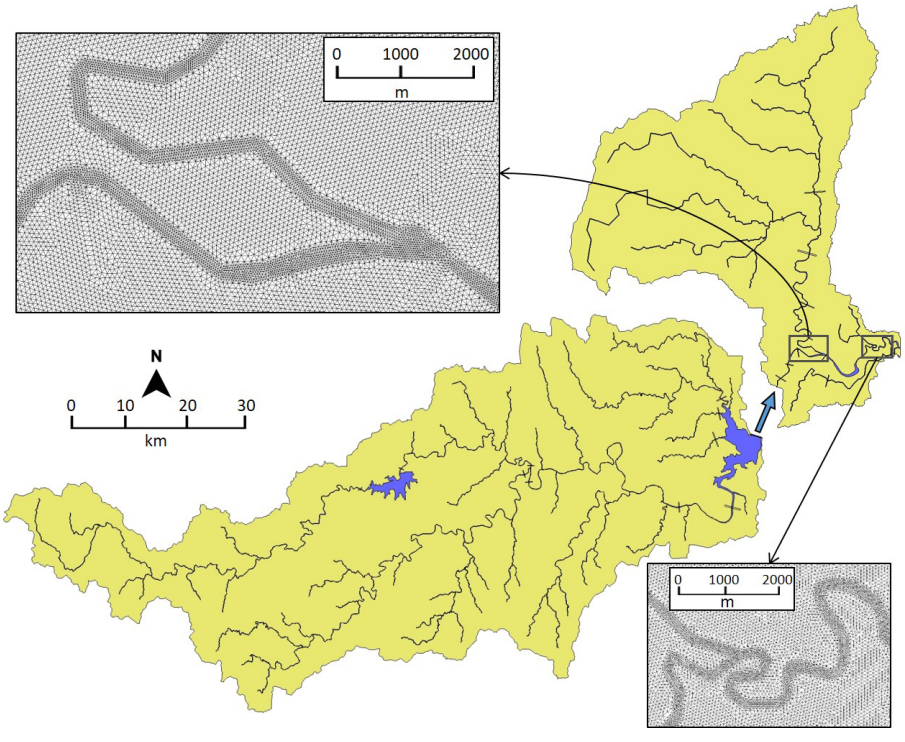

Figure 6. Implementation in Iber of the Umbeluzi Catchment. Geometry of the U-PLD and D-PLD models and details of the numerical discretisation.

Table 2. Manning coefficient assigned to each land cover considered in the ESA WorldCover 10m 2021 v200.

Land cover	Manning ($s\,m^{-1/3}$)
Tree cover	0.070
Shrubland	0.060
Grassland	0.035
Cropland	0.050
Built-up areas	0.100
Bare/sparse vegetation	0.030
Herbaceous wetland	0.040
Permanent water bodies	0.025

the river network in detail or to define the water bodies precisely, such as the reservoirs. Therefore, the value of CN in the river network and reservoirs was imposed manually to 100 in order to force the infiltration to 0 in these areas.

Manning's coefficient was defined by considering eight different land covers: tree cover, shrubland, grassland, cropland, built-up areas, bare/sparse vegetation, herbaceous wetland, and permanent water bodies. Their spatial distribution with a resolution of 10 m was obtained from the ESA WorldCover 10m 2021 v200 land cover map (Fig. 4), except for the permanent water bodies, which were assigned manually in order to achieve a more precise definition of their geometry than that given by the ESA WorldCover 10m 2021 v200. The Manning coefficients assigned to each land use are shown in Table 2.

Rainfall intensity fields were defined in the model with spatial and temporal resolutions of 10 km and 30 min respectively, using raster files obtained directly from the GPM-IMERG database (Sect. 3.1.2). The numerical simulation extended from 6 February 2023 at 00:00 UTC to 15 February 2023 at 00:00 UTC (9 d).

Regarding boundary conditions, in the U-PLD model only one outlet boundary was defined at the dam location, where the water surface elevation of the reservoir was imposed as a constant value during the whole simulation. As for the D-PLD model, inlet and outlet boundaries were defined at the dam location and at the catchment outlet respectively. At the inlet boundary, different inflow hydrographs were imposed for each modelling scenario, as described in Sect. 3.4. At the outlet boundary a supercritical flow condition was imposed after verification that this condition did not affect the results of the flood extent in Boane.

The model was run on a standard desktop with a NVIDIA GeForce RTX 3080 Ti, which is an affordable GPU. With this hardware configuration, the simulations in the U-PLD and D-PLD models took around 25 and 15 min of computational time to reproduce the whole period of 9 d (i.e. each model runs about 600 times faster than real time).

3.3 Data for model validation

3.3.1 Inflow and outflow discharges from the PL reservoir

The inflow and outflow daily discharges from the PL reservoir from 6 to 15 February 2023, as well as the water surface elevation in the reservoir, were provided by ARA-Sul and are shown in Fig. 7. While the outflow hydrograph was controlled by ARA-Sul through the operation of the dam spillways and outlets during the event, the inflow hydrograph was derived from a daily mass balance in the reservoir, considering the controlled outflow and the daily evolution of its water surface elevation. Each discharge value in Fig. 7 was computed daily at 07:00 UTC of the current day and corresponds to the average discharge over the previous 24 h, while the water surface elevation values correspond to the actual water level in the reservoir at 07:00 UTC of the current day.

At the beginning of the event the reservoir was almost full. The water surface elevation was 45.76 m (corresponding to a storage volume of 336 hm^3 and 87 % of its storage capacity), very near to its normal pool level (NPL), which is 47.00 m and 385 hm^3. Thus, when the inflow discharge began to rise markedly, on 9 February 2023, the reservoir spillways were opened to their maximum capacity (circa 2850 $m^3\,s^{-1}$), releasing around 250 hm^3 per day (i.e. around 65 % of the reservoir's storage capacity). This situation was maintained for 2 d, until the inflow discharge began to decrease. Over these 2 d the daily average inflow discharge was 3900 and 2700 $m^3\,s^{-1}$ respectively, leading to an increase in the reservoir's water level to 48.50 m, i.e. 1.5 m above its NPL and just 1.05 m below its maximum pool level (MPL) for the design flood. At the end of the event, the water storage in the reservoir was similar to the initial level, corresponding to a water surface elevation of roughly 46 m.

3.3.2 Maximum water depths

On 20–21 March 2023, the neighbourhoods of the Boane district most damaged by the flood were visited by technicians from the regional water administration ARA-Sul in order to estimate the level reached by the waters during the flood event. During this field work, inundation marks on buildings and other infrastructure were identified. At each point identified, the maximum water depth reached during the flood was estimated as the difference between the elevation of the inundation mark and the terrain at that location. A total of 20 water marks were thus identified; their locations are shown in Fig. 8.

3.3.3 Water extent estimated from Sentinel-1 data

The ESA satellite Sentinel-1A captures Earth images with a 12 d repeat cycle. It is equipped with a C-band advanced synthetic aperture radar (SAR) that enables it to capture images under cloudy or rainy weather conditions, during both day

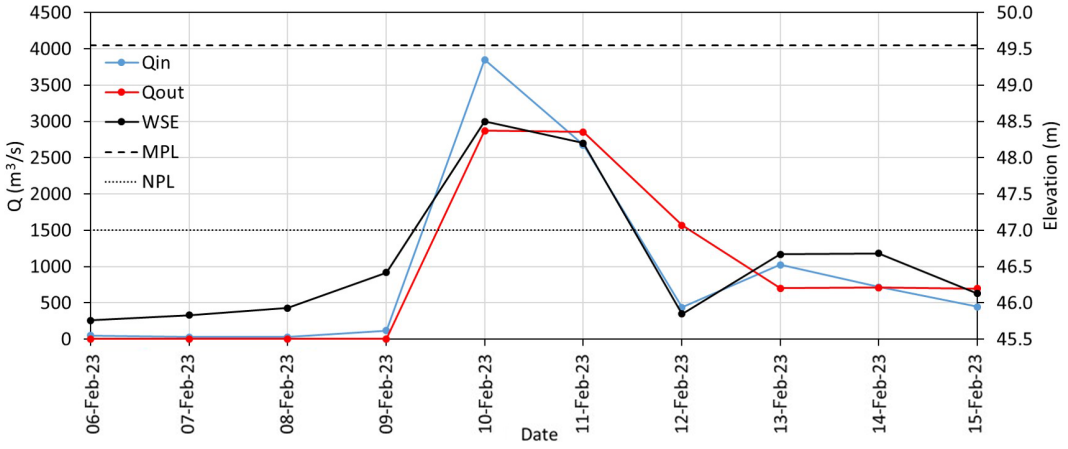

Figure 7. Daily inflow (Q_{in}), daily outflow (Q_{out}), and water surface elevation (WSE) in the PL reservoir during the flood event. The normal pool level and maximum pool level (NPL and MPL) are also provided for reference. Daily discharges correspond to the average over the previous 24 h.

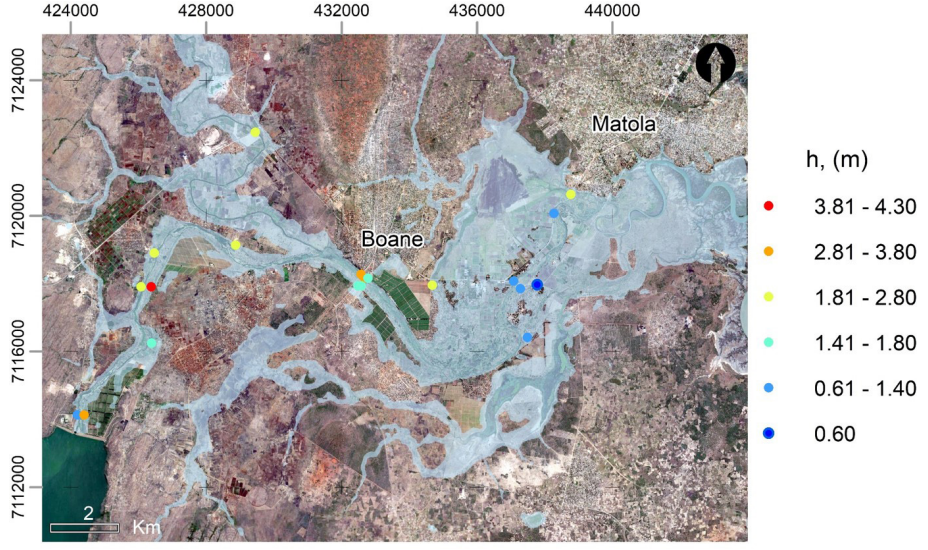

Figure 8. Location of the points at which the maximum water depth during the flood was estimated from field observations of the marks left by the water. The colour of the dots indicates the maximum water depth estimated. The shaded area represents the maximum flood extent for the MS1 scenario. Background image: © Google Earth version 7.3.6.9345, http://www.earth.google.com (last access: 13 April 2023).

and night, and is hence very suitable for estimating the extent of the water surface (Nemni et al., 2020). In Sentinel-1A images, water can be distinguished from the surrounding terrain because its different roughness causes a different level of backscatter (Kuntla and Manjusree, 2020).

During the storm event of February 2023, the only available image from Sentinel-1 covering the AOI was taken on 14 February 2023 at 03:20 UTC, and it was used in this study to estimate the water extent with a pixel resolution of 10 m. The Sentinel Application Platform (SNAP) toolkit developed by the ESA for processing SAR-C images (Zuhlke et al., 2015) was used for this purpose. A pixel-based comparison with the water extent obtained with Iber at the same time was carried out using the following performance indices (Bennett et al., 2013; Bermudez et al., 2019; Costabile et al., 2020; Grimaldi et al., 2016):

$$\mathrm{HR} = \frac{\mathrm{TP}}{\mathrm{TP}+\mathrm{FN}}, \quad \mathrm{FAR} = \frac{\mathrm{FP}}{\mathrm{TP}+\mathrm{FP}}, \quad \mathrm{CSI} = \frac{\mathrm{TP}}{\mathrm{TP}+\mathrm{FP}+\mathrm{FN}}, \tag{4}$$

where HR is the hit rate (proportion of the area observed as flooded in the satellite image that the model also predicts as flooded), FAR is the false alarm ratio (proportion of the area predicted as flooded by the model that has been observed as dry in the satellite image), CSI is the critical success index, TPs are the true positives (number of grid cells correctly predicted as flooded), FPs are the false positives (number of cells that the model predicted as flooded but were observed

Table 3. Maximum water depths during the flood, estimated from field observations of water marks at several locations in the Boane district. The terrain elevation retrieved from the Copernicus GLO-30 DEM is also shown. X and Y coordinates correspond to UTM zone 36S.

ID	X (m)	Y (m)	h field (m)	Z_b DEM (m)
1	424 197.7	7 114 128.6	1.3	28.3
2	424 397.7	7 114 129.8	3.7	23.1
3	426 076.4	7 117 905.1	2.6	17.9
4	426,471.0	7 118 904.1	2.5	16.4
5	428 870.8	7 119 138.9	2.6	15.6
6	429 453.1	7 122 464.6	2.8	10.3
7	432 577.0	7 118 272.5	3.8	8.5
8	432 677.6	7 118 162.3	3.4	7.2
9	432 777.6	7 118 162.8	1.6	11.3
10	432 478.7	7 117 939.8	1.8	12.6
11	432 578.7	7 117 940.3	1.6	10.6
12	426 385.9	7 116 245.5	1.8	18.4
13	426 376.5	7 117 906.8	4.3	17.1
14	434 679.4	7 117 951.0	2.3	6.9
15	437 079.7	7 118 073.5	1.4	7.1
16	437 280.8	7 117 853.0	1.1	9.3
17	437 487.8	7 116 414.2	1.3	8.2
18	437 780.5	7 117 966.1	0.6	6.7
19	438 270.7	7 120 072.7	1.2	7.1
20	438 768.3	7 120 628.8	2.4	3.0

as dry), and FNs are the false negatives (number of cells predicted as dry but observed as flooded). The three ratios vary between 0 and 1. The HR penalises underprediction, and its optimal value is 1, meaning that all the areas observed as flooded are correctly identified. On the other hand, the FAR penalises overprediction, and its optimal value is 0, meaning that all the areas predicted as flooded by the model are also identified as flooded by the satellite image. The CSI penalises both overprediction and underprediction. Thus, to have a CSI close to 1 (its optimal value), the model prediction must match the satellite observation. As the model overpredicts or underpredicts the observations, the value of the CSI will diminish towards 0.

3.4 Modelling scenarios

The total discharge arriving at Boane originates from both the PL reservoir and the unregulated D-PLD subbasin. The reservoir's outflow hydrograph can, to a certain degree, be controlled by its management strategy, but this is not the case with the runoff originating from the D-PLD subbasin, in that there is not any regulation structure there. In order to better understand and quantify the contributions of both sources of flooding to the total hydrograph arriving at Boane, three flooding scenarios were reproduced with the numerical model (Table 4).

MS1 reproduces the flood event that took place in February 2023, considering the actual management of the PL reservoir on those dates. The purpose of this scenario is to validate the model predictions and to reproduce the flood extent and depths in Boane during the event. Thus, the actual outflow discharge from the PL reservoir (Fig. 7) was imposed as an inlet discharge at the location of the PL dam in the D-PLD model.

MS2 is a prediction of what would have happened if the PL reservoir had not existed. The aim here is to quantify the effective flood control exerted by the PL dam, by comparing the MS2 results with those of MS1 in terms of flood hazard in Boane. In this case, the inlet discharge at the location of the PL dam in the D-PLD model is equal to the outflow discharge computed in the U-PLD model, as schematised in Fig. 6.

Finally, MS3 predicts what would have happened if the PL reservoir had been able to retain and control the total inflow arriving there during the storm event. As noted in Sect. 3.3.1, this is not possible with the dam itself, since the volume of water arriving at the reservoir between 11–14 February 2023 roughly doubled its maximum capacity. The aim here is to quantify the maximum reduction in flood hazard that could have been achieved in Boane if a far larger reservoir than PL had existed. In this scenario, the inlet discharge in the D-PLD model is null, and the only source of flooding is the runoff generated in the D-PLD subbasin, the greatest contribution to which is from the Movene River basin (Fig. 1).

4 Results and discussion

4.1 Model validation: scenario MS1

The ability of the proposed modelling approach to reproduce the flood event that took place on 9–13 February 2023 in the Umbeluzi Catchment was assessed by comparing the predicted and observed values of (1) the inlet hydrograph into the PL reservoir, (2) the maximum depths reached by the water at the locations shown in Table 3, and (3) the extension of the water in Boane at the time when the available Sentinel-1 image was taken (14 February 2023 at 03:20 UTC).

4.1.1 Hydrographs into the PL reservoir

Figure 9 shows the observed and computed daily average discharge during the flood event. The numerical agreement with the observations is very good, with a coefficient of determination of $R^2 = 0.96$ and no relevant trend in the results. Therefore, the model parametrisation, and more specifically the assumption of wet AMC conditions in order to compute the infiltration losses with the SCS-CN method, can be considered a plausible hypothesis that effectively represents the response of the catchment during the flood event of February 2023.

The hourly discharge into the PL reservoir computed with Iber, which is also represented in Fig. 9, shows that the peak

Table 4. Description of the modelling scenarios analysed.

Modelling scenario	Brief description	Purpose	Forcing in the D-PLD model
MS1	Actual flood event	Validate the model	Rainfall + regulated outflow from the PL dam
MS2	No PL reservoir	Comparison with MS1 to quantify the flood control exerted by the PL dam	Rainfall + natural outflow from the U-PLD model
MS3	Reservoir with unlimited storage	Quantify the maximum reduction in flood hazard that could be achieved with a far larger reservoir than PL	Rainfall

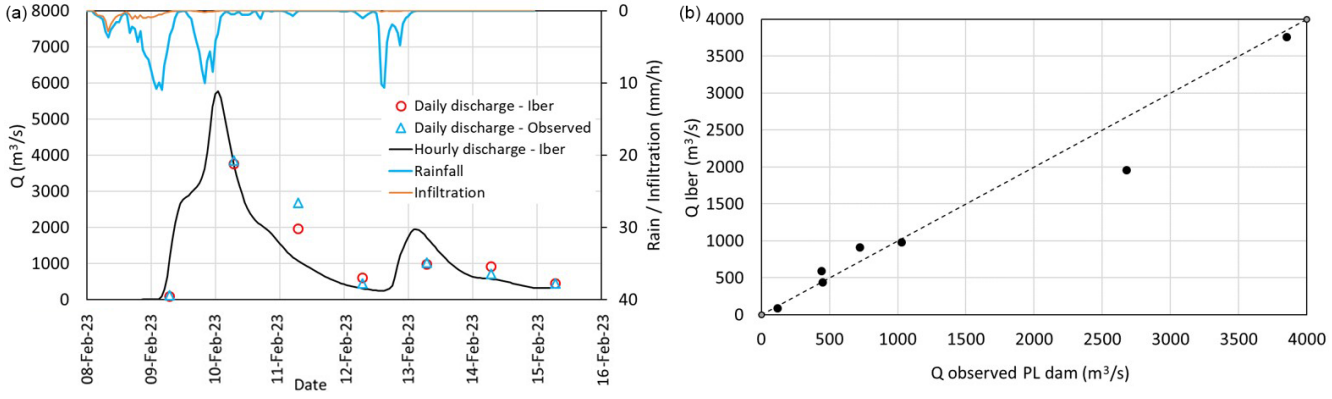

Figure 9. Observed and modelled inlet discharges into the PL reservoir. Time series of daily and hourly discharge **(a)**, simulated hourly discharge (top right), and observed vs. simulated average daily discharge showing the identity line **(b)**.

hourly discharge flowing into the reservoir (5700 $m^3 s^{-1}$) was almost 50 % higher than the maximum daily discharge (3780 $m^3 s^{-1}$).

4.1.2 Maximum water depths

The most vulnerable areas in terms of flood damage are the floodplains located between the PL dam and the surroundings of Maputo, and it is thus in this area where the analysis of flood extent and maximum water depths was focused. This area of interest, indicated as AOI in Fig. 10, receives the outflow discharge from the PL reservoir, as well as the surface runoff generated by the rainfall falling in the D-PLD subbasin, shown as a shaded area in Fig. 10. Figure 10 also shows the hydrographs computed at three river cross-sections located within the AOI, around the confluence of the Umbeluzi and Movene rivers.

The outflow hydrograph from the reservoir is barely transformed when it propagates 8.16 km from the PL dam to cross-section S3, with a peak discharge of almost 3000 $m^3 s^{-1}$ attained on 10 February at 09:00 UTC and maintained for 1 d, until 11 February at 09:00 UTC. The peak discharge of the hydrograph generated on the D-PLD subbasin is slightly lower (around 2550 $m^3 s^{-1}$) and occurs about 20 h earlier (on 9 February 2023 at 13:00 UTC). Therefore, the total contribution of the D-PLD subbasin to the peak discharge arriving at Boane (cross-section S2) is relatively small, increasing the peak discharge roughly from 3000 to 3500 $m^3 s^{-1}$. On the other hand, it generates a second peak in the hydrograph at the end of the event, increasing the maximum discharge on 13 February 2023 from 750 to 2400 $m^3 s^{-1}$ (Fig. 10). This second peak of discharge is due to a second precipitation peak on 12 February 2023 (Fig. 9), which is controlled by the reservoir in the U-PLD basin but not in the unregulated D-PLD basin.

There are no field estimations of the discharge arriving at the Boane district during the flood event, and hence the previous hydrographs cannot be compared to observations. Only the maximum water depths estimated during the post-event field campaign at 20 locations in the AOI (Sect. 3.2.2) have been used to assess the numerical predictions (Fig. 11). The comparison between the observed and predicted water depths has a mean error (ME) of 0.50 m and a mean absolute error (MAE) of 1.06 m. The MAE is of the same order of magnitude as the vertical accuracy of the Copernicus DEM, which was estimated to have a global root mean square error (RMSE) of 1.7 m for terrain slopes lower than 20 % (AIRBUS, 2020). Moreover, the positive ME means that the numerical predictions of the maximum water surface elevation

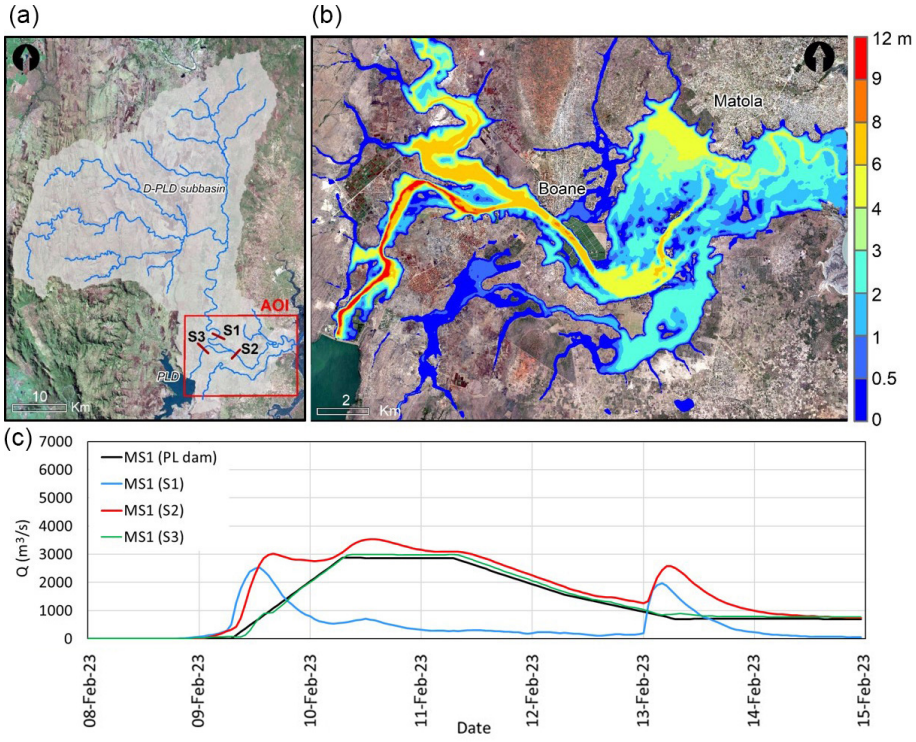

Figure 10. Extension of the D-PLD subbasin with its main river network and the location of cross-sections S1–S3 **(a)**, map of maximum water depth in the AOI **(b)**, and hydrographs computed with Iber at several cross-sections located around the confluence of the Umbeluzi and Movene rivers for the MS1 scenario. Background images: © Google Earth version 7.3.6.9345, http://www.earth.google.com (last access: 13 April 2023).

have a positive bias with regard to the field estimations. Several reasons might explain the positive bias. First, within the main river channels the estimated terrain elevation given by the DEM may be higher than the real elevation due to its limited spatial resolution and the fact that satellite-derived DEMs do not capture the terrain elevation below the water level. This issue cannot be solved in the absence of a huge amount of field topographic data, which are not available in data-scarce regions. Second, the fact of having chosen a CN associated with wet AMC might have led to an overestimation of its value and in turn to a subestimation of the infiltration rate. As mentioned in Sect. 3.1.4, we considered wet AMC conditions because the 5 d antecedent rainfall depth was greater than 50 mm. Third, the water marks identified in the field work might underestimate the real maximum level reached by the water, since the fact that there is a mark at a certain location means that the water reached that level, but the flood might have reached a higher level without leaving a significant mark. These three factors might have contributed, to different degrees, to the deviations shown in Fig. 11, the first two being probably the most relevant. Despite these limitations, it can be concluded that the numerical predictions of maximum water depths during the event in the AOI follow the same trend as the observations (Fig. 11).

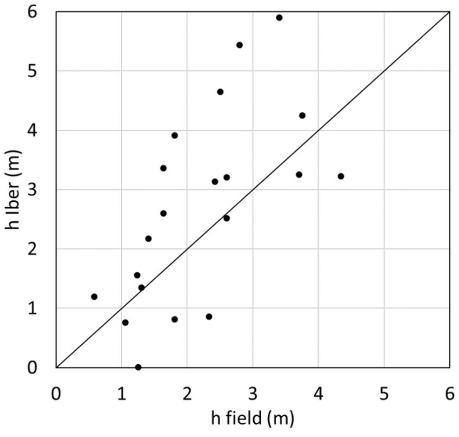

Figure 11. Observed vs. computed maximum water depths at the locations indicated in Fig. 8. The identity line (solid black) is shown.

4.1.3 Flood extent

The only available satellite image during the flood event was taken on 14 February at 03:00 UTC. At that time the peak discharge had already passed, and the flood was receding. The discharge at cross-section S2, estimated from the numerical model, was 915 $m^3 s^{-1}$, almost 4 times lower than the maxi-

mum discharge reached at this cross-section during the whole event. Nonetheless, several floodplains were still covered by water in the AOI, as shown in Fig. 12, which shows the water extent at that time, as estimated using Iber (assuming areas with a water depth greater than 0.1 m to be flooded) and the Sentinel-1 image, as well as from the overlapping between these.

Most of the observed flooded areas are correctly predicted by the model, which shows an HR of 0.96. On the other hand, the model predicts several flooded areas that are not identified from the analysis of the Sentinel-1 image, the FAR being 0.37 and the CSI being 0.67. These results indicate that the model tends to overestimate the extent of the flood. A good portion of the overestimation occurs in the floodplains of the Movene tributary, upstream of its confluence with the Umbeluzi. At the control point located in this region (ID 6 in Tables 3 and 5), the model largely overpredicts the water depth (5.4 m versus 2.8 m). This reach comes directly from the northern D-PLD subbasin, and thus the flood extent in its floodplains is barely affected by the discharge of the dam, so the overestimation of the water depth and flood extent is probably an effect of an underestimation of the infiltration rate in the model.

The fact that the riparian vegetation can mask the water surface in floodplains with small water depths can also contribute to the difference between the modelled and satellite-derived maps, increasing the number of false positives and thus the FAR. This limitation of satellite-derived flood maps might be, in certain cases, alleviated by the use of exclusion maps that identify the regions in which the satellite-derived estimation is not reliable (Zhao et al., 2021; Di Mauro et al., 2021).

4.2 Mitigation of the flood hazard by the PL reservoir: scenario MS2

During the flood event, from 8 to 15 February, the PL reservoir received over 800 hm^3 from its upstream basin. Around 40 % of this volume (330 hm^3, which is almost the maximum storage capacity of the whole reservoir) reached the reservoir within 24 h on 10 February 2023. Thus, the PL dam had to release water to its maximum capacity (circa 3000 $m^3 s^{-1}$) and storage capacity for reasons of structural safety for 2 d (10–11 February 2023). This high discharge, maintained over the course of 2 d, had an effect on the flood extent in the district of Boane, leading to strong criticism from the local communities and the press of the reservoir's management. However, due to the high inflow discharges relative to the reservoir storage capacity, there was no margin to diminish the outflow peak discharge.

Nevertheless, the reservoir had a net positive effect on the impact of the flood, reducing the extent of the affected areas, as shown in Fig. 13, which compares the water extent computed under the real management of the reservoir during the event (scenario MS1) with the water extent that would have taken place if the PL reservoir had not existed (scenario MS2). In the absence of the reservoir (i.e. no flood control at all), the peak discharge of the hydrograph arriving at the district of Boane (cross-section S2) would have reached 6000 $m^3 s^{-1}$, which is 70 % higher than the discharge computed under scenario MS1 (3500 $m^3 s^{-1}$). We note that the volume of the hydrographs arriving at Boane under scenarios MS1 and MS2 is roughly the same (Fig. 13), and thus the effect of the dam was to redistribute the total volume of water arriving at the reservoir over time.

In terms of maximum flood extent and water depth during the event, the effect of the reservoir was to reduce the flooded surface in the AOI from 94 to 84 km^2, while the average water depth in the AOI was reduced from 2.9 to 2.1 m (Table 5).

In order to relate the results of scenario MS2 to the maximum discharges arriving at Boane if the PL dam had not existed, we retrieved the maximum annual discharges at cross-section S2 from 1955 to 1986 from Lacamurima (2003). In that cross-section there was a stream gauge, known as Boane hydrometric station E-8, which was in operation until 1986 when the PL dam was built. The maximum discharge registered in the E-8 Boane station was 7250 $m^3 s^{-1}$ on 30 January 1984. It is interesting to note that this value is of the order of magnitude of the peak discharge computed for the February 2023 flood under scenario MS2 (i.e. in the absence of the PL reservoir).

Table 5. Water depth at the 20 control points, computed with the numerical model, in scenarios MS1, MS2, and MS3.

ID	h_{max} (m)		
	MS1	MS2	MS3
1	0.0	0.6	0.0
2	3.2	5.0	0.0
3	3.2	5.3	0.0
4	4.6	6.7	0.4
5	2.5	3.6	1.6
6	5.4	6.6	5.3
7	4.3	5.7	3.2
8	6.0	7.6	5.0
9	2.6	3.8	1.5
10	0.8	2.3	0.4
11	3.4	4.9	2.6
12	3.9	6.5	0.2
13	3.2	5.3	0.0
14	0.9	1.6	0.5
15	2.2	2.6	1.9
16	0.8	0.9	0.5
17	1.4	1.6	0.9
18	1.2	1.6	1.0
19	1.6	2.3	1.2
20	3.1	3.9	2.5
Mean	2.7	3.9	1.4

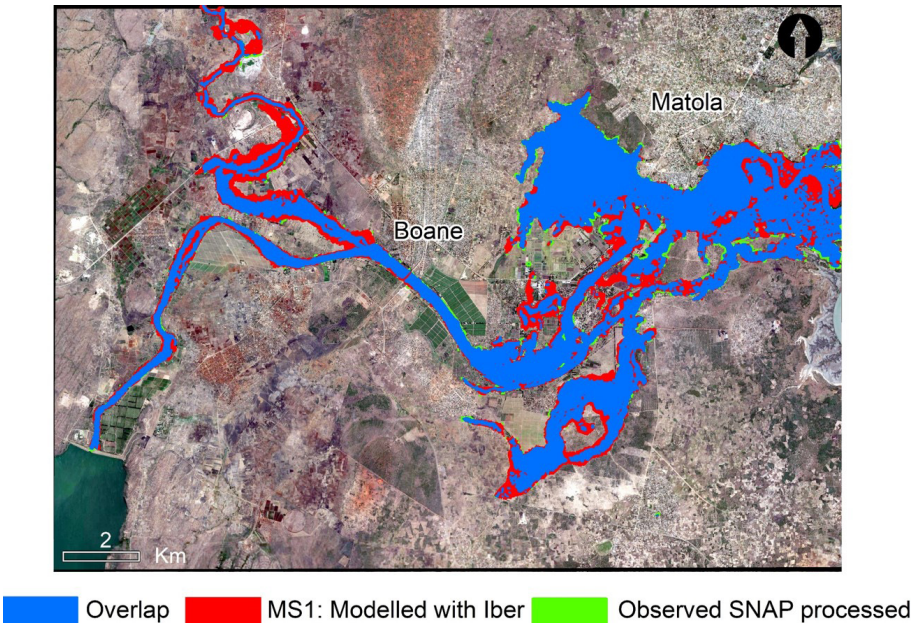

Figure 12. Overlapping (blue) between the modelled (red) and satellite-derived (green) flood extent in the AOI on 14 February 2023 at 03:20 UTC. Background image: (©) Google Earth version 7.3.6.9345, http://www.earth.google.com (last access: 13 April 2023).

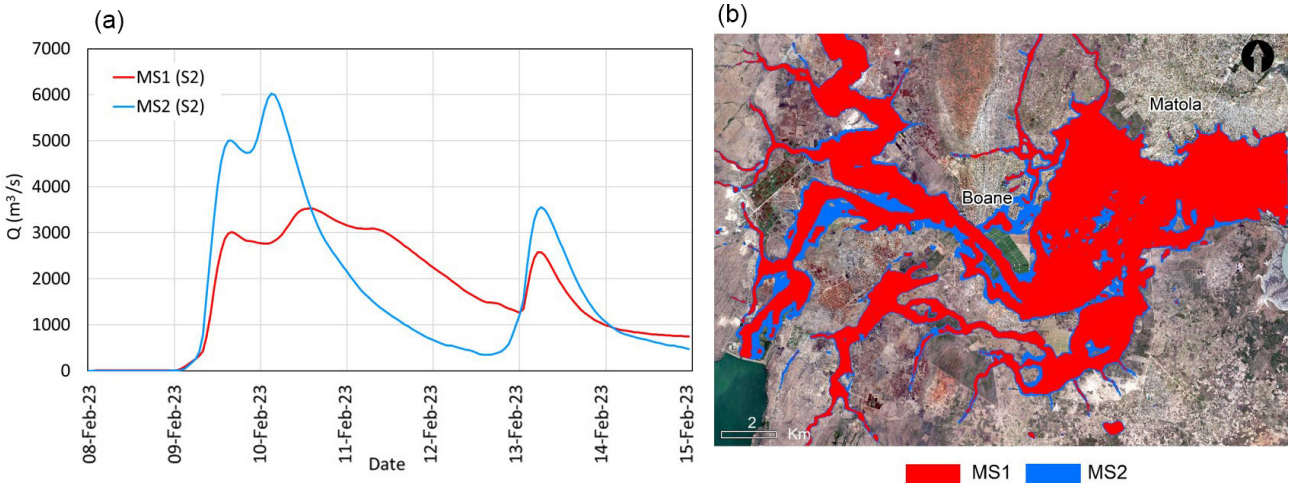

Figure 13. Hydrograph arriving at Boane **(a)** and flood extent in the AOI **(b)**, under scenarios MS1 (actual management of the reservoir during the flood event) and MS2 (absence of PL reservoir) scenarios. Background image: © Google Earth version 7.3.6.9345, http://www.earth.google.com (last access: 13 April 2023).

4.3 Flooding from the unregulated subbasin: scenario MS3

Figure 14 shows the water depth maps computed in the AOI under scenarios MS1 (actual flood) and MS3 (contribution only from the unregulated D-PLD subbasin). If the dam had not spilled any water at all during the flood event, the peak discharge in the district of Boane would have diminished from roughly 3500 to 2300 $m^3 s^{-1}$, the flooded area within the AOI would have been 76 km^2 instead of 84 km^2, and the average water depth in the AOI would have been 1.6 m instead of 2.1 m (Table 6). Despite this virtual reduction in the flood hazard, the damage to the population would have remained very severe, since many populated areas in the region would still have been flooded to significant water depths, as shown in Fig. 14. In any case, it should be stressed that, regardless of how the dam was managed, it would never have been possible to achieve scenario MS3 for the flood of February 2023 due to the limited storage capacity of the reservoir.

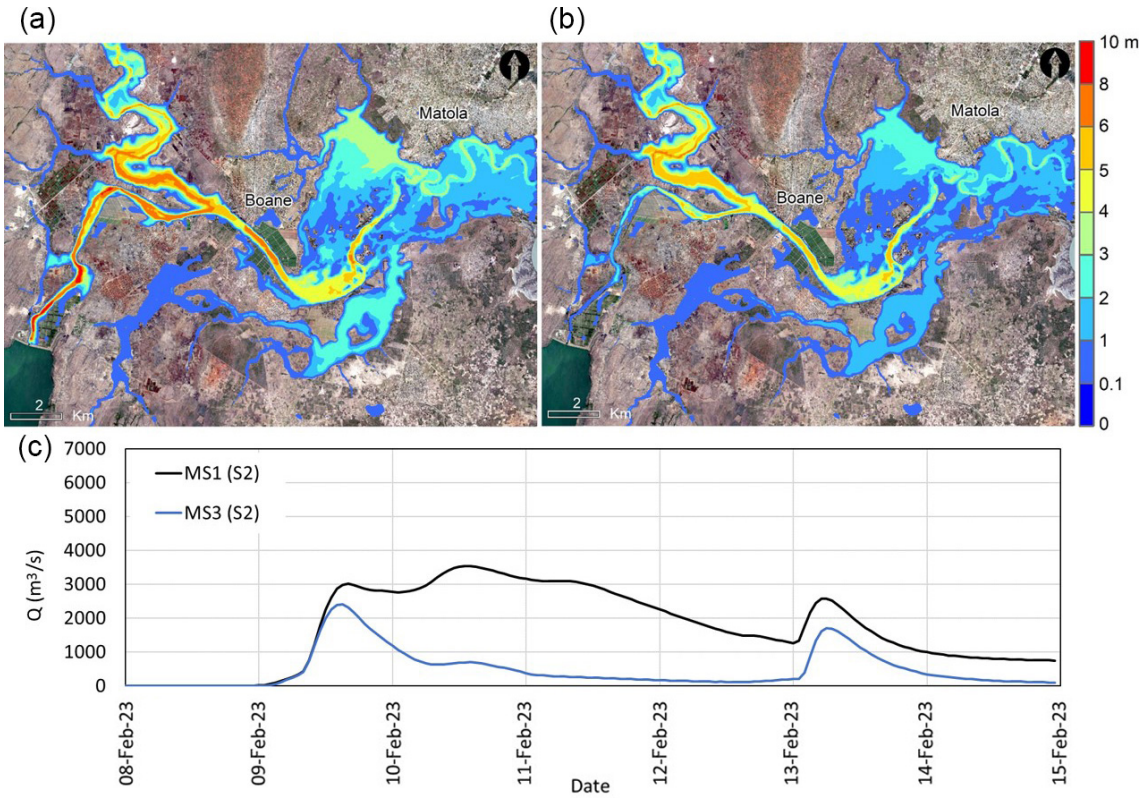

Figure 14. Water depth maps computed under scenarios MS1 **(a)** and MS3 **(b)**. The hydrographs computed in cross-section S2 for both scenarios are also shown. Background images: © Google Earth version 7.3.6.9345, http://www.earth.google.com (last access: 13 April 2023).

Table 6. Results of maximum discharge in cross-section S2, flooded area, and average depth in the AOI for the three modelling scenarios.

Scenario	Q_{max} in S2 ($m^3\ s^{-1}$)	Flooded area in AOI (km^2)	Average depth in AOI (m)
MS1	3500	84	2.1
MS2	6000	94	2.9
MS3	2300	76	1.6

5 Conclusions

The numerical simulation of the flood that took place on 11–14 February 2023 in the Umbeluzi River basin confirms that integrated hydrological–hydraulic models based on the 2D-SWE combined with global data sources are efficient tools in reproducing the flood hazard during extreme rainfall events in data-scarce catchments of several thousands of square kilometres. The model used here (a GPU-enhanced solver for the 2D-SWE including rainfall and infiltration processes) was able to reasonably reproduce the peak discharge and flood extent during the event, using only satellite-derived products of rainfall, topography, land use, and curve number as input data, all of which are available on a global scale. The maximum water depths estimated in a field survey after the flood event were not so accurately reproduced by the model. This can be attributed to a number of factors, such as the uncertainty in the currently available global DEMs, the uncertainty in the numerical parametrisation of the infiltration losses, and the uncertainty in the water depths estimated in the post-event field survey.

The methodology followed in this work is reproducible anywhere but not necessarily with the same rate of success in all cases. It is expected to perform better in extreme rainfall events over wet terrains, occurring in relatively large catchments with a low rate of anthropisation, as this was the case in the event analysed in this work.

The spatial rainfall pattern over the basin shows that the highest cumulative rainfall depth during the event occurred around the PL reservoir, near the outlet of the U-PLD subbasin, contributing to reducing the response time of the basin and increasing the peak discharge into the PL dam. The quick response of the basin did not give any possibility of operating the dam spillways by releasing water with the aim of providing more storage available in the reservoir to mitigate the peak flow. Nevertheless, considering the basin size, a different rainfall distribution may provide this operational time

if a hydrologic–hydraulic operational tool is implemented to forecast river discharges in real time, which would constitute best practice for reservoir flood management.

In addition to the management of the PL dam during the flood event, two additional scenarios were modelled: a case of the reservoir not existing (i.e. no flood control by the dam) and where the reservoir would control all the inflow hydrographs. From the results of these scenarios, it can be concluded that the PL reservoir contributed to the reduction of the flood hazard in Boane during the February 2023 event, reducing the peak discharge from 6000 to 3500 $m^3 s^{-1}$, the flooded area from 94 to 84 km^2, and the average depth from 2.9 to 2.1 m. Even if there had been a reservoir capable of absorbing the entire volume of the hydrograph generated in its upstream basin, the extension of the inundation in the AOI would have been 76 km^2, with an average depth of 1.6 m.

The results presented here show that it is currently possible to delineate flood hazard maps in data-scarce regions under different scenarios using freely available numerical tools and input data, thus contributing to more efficient flood risk management. However, the accuracy of the water depth results might be limited by the spatial resolution and accuracy of the global DEMs currently available. Future enhancements in these global topography products will further improve the accuracy of the modelling approach presented here.

Data availability. The DEM of the Umbeluzi Catchment is publicly available via the Copernicus Space Component Data Access PANDA Catalogue (https://panda.copernicus.eu/web/cds-catalogue, ESA, 2023). The rainfall data are publicly available via the Goddard Earth Sciences Data and Information Services Center (GES DISC) from NASA (2023; https://disc.gsfc.nasa.gov). The ESA WorldCover 10m 2021 v200 map is publicly available via the ESA GlobCover Portal (http://due.esrin.esa.int/page_globcover.php, ESA, 2021). The curve number map is publicly available from the Figshare open repository (https://doi.org/10.6084/m9.figshare.7756202.v1, Jaafar and Ahmad, 2019). The satellite image from Sentinel-1A is publicly available via the Copernicus Open Access Hub (https://scihub.copernicus.eu/dhus, Copernicus and ESA, 2023). The numerical simulations were done with Iber v3.1 software, which can be downloaded free of charge from http://www.iberaula.com (Universidade da Coruña and Universitat Politècnica de Catalunya CEDEX, 2024).

Author contributions. MA built the numerical model and performed all the numerical simulations. LC supervised and revised the numerical model. LC and MA analysed the numerical results and their validation with the observed data. LC and MA wrote the first draft of the manuscript. JP revised the paper.

Competing interests. The contact author has declared that none of the authors has any competing interests.

Disclaimer. Publisher's note: Copernicus Publications remains neutral with regard to jurisdictional claims made in the text, published maps, institutional affiliations, or any other geographical representation in this paper. While Copernicus Publications makes every effort to include appropriate place names, the final responsibility lies with the authors.

Acknowledgements. The authors would like to thank the head of the Water Resources Department of the Regional Water Administration of southern Mozambique, Lizete Días, and their technicians Ernesto Tivane and Leonel Bila, for the data provided from the Pequenos Libombos dam, as well as for the field work carried out in the Boane district in the days following the flood. The authors also acknowledge Victor Penas and the management staff from the AquaMoz project (Augas de Galicia/Xunta de Galicia, Cooperación Galega, and Ingeniería sin Fronteras Galicia) for additional support provided.

Review statement. This paper was edited by Daniela Molinari and reviewed by Alessio Radice and two anonymous referees.

References

AIRBUS: Copernicus DEM Validation Report (v3.0), 23 pp., https://doi.org/10.5270/ESA-c5d3d65, 2020.

Bayburt, S., Kurtak, A. B., Büyüksalih, G., and Jacobsen, K.: Geometric accuracy analysis of WorldDEM in relation to AW3D30, SRTM and ASTER GDEM2, International Archives of the Photogrammetry, Remote Sensing and Spatial Information Sciences-ISPRS Archives, 42, 211–217, 2017.

Bennett, N. D., Croke, B. F. W., Guariso, G., Guillaume, J. H. A., Hamilton, S. H., Jakeman, A. J., Marsili-Libelli, S., Newham, L. T. H., Norton, J. P., Perrin, C., Pierce, S. A., Robson, B., Seppelt, R., Voinov, A. A., Fath, B. D., and Andreassian, V.: Characterising performance of environmental models, Environ. Model. Softw., 40, 1–20, https://doi.org/10.1016/j.envsoft.2012.09.011, 2013.

Bermúdez, M., Cea, L., and Puertas, J.: A rapid flood inundation model for hazard mapping based on least squares support vector machine regression, J. Flood Risk Manag., 12, e12522, https://doi.org/10.1111/jfr3.12522, 2019.

Bladé, E., Cea, L., Corestein, G., Escolano, E., Puertas, J., Vázquez-Cendón, M. E., Dolz, J., and Coll, A.: Iber: herramienta de simulación numérica del flujo en ríos, Rev. Int. Metod. Numer., 30, 1–10, https://doi.org/10.1016/j.rimni.2012.07.004, 2014.

Caviedes-Voullième, D., Morales-Hernández, M., Norman, M. R., and Özgen-Xian, I.: SERGHEI (SERGHEI-SWE) v1.0: a performance-portable high-performance parallel-computing shallow-water solver for hydrology and environmental hydraulics, Geosci. Model Dev., 16, 977–1008, https://doi.org/10.5194/gmd-16-977-2023, 2023.

Cea, L. and Blade, E.: A simple and efficient unstructured finite volume scheme for solving the shallow water equations in overland flow applications, Water Resour. Res., 51, 5464–5486, https://doi.org/10.1002/2014WR016547, 2015.

Cea, L., Garrido, M., Puertas, J., Jácome, A., del Río, H., and Suárez, J.: Overland flow computations in urban and industrial catchments from direct precipitation data using a two-dimensional shallow water model, Water Sci. Technol., 62, 1998–2008, https://doi.org/10.2166/wst.2010.746, 2010.

Cea, L., Álvarez, M., and Puertas, J.: Estimation of flood-exposed population in data-scarce regions combining satellite imagery and high resolution hydrological-hydraulic modelling: A case study in the Licungo basin (Mozambique), J. Hydrol. Reg. Stud., 44, 101247, https://doi.org/10.1016/j.ejrh.2022.101247, 2022.

Copernicus and ESA: The Copernicus Data Space Ecosystem, Copernicus and ESA [data set], https://scihub.copernicus.eu/dhus (last access: 1 March 2023), 2023.

Costabile, P., Costanzo, C., Ferraro, D., Macchione, F., and Petaccia, G.: Performances of the new HEC-RAS version 5 for 2-D hydrodynamic-based rainfall-runoff simulations at basin scale: comparison with a state-of-the art model, Water, 12, 2326, https://doi.org/10.3390/w12092326, 2020.

Di Mauro, C., Hostache, R., Matgen, P., Pelich, R., Chini, M., van Leeuwen, P. J., Nichols, N. K., and Blöschl, G.: Assimilation of probabilistic flood maps from SAR data into a coupled hydrologic–hydraulic forecasting model: a proof of concept, Hydrol. Earth Syst. Sci., 25, 4081–4097, https://doi.org/10.5194/hess-25-4081-2021, 2021.

ESA: PANDA Catalogue, ESA [data set], https://panda.copernicus.eu/web/cds-catalogue (last access: 1 March 2023), 2023. ESA: GlobCover, ESA [data set], http://due.esrin.esa.int/page_globcover.php (last access: 1 March 2023), 2021.

Fraga, I., Cea, L., and Puertas, J.: Effect of rainfall uncertainty on the performance of physically-based rainfall-runoff models, Hydrol. Process., 33, 160–173, https://doi.org/10.1002/hyp.13319, 2019.

Funk, C., Peterson, P., Landsfeld, M., Pedreros, D., Verdin, J., Shukla, S., Husak, G., Rowland, J., Harrison, L., Hoell, A., and Michaelsen, J.: The climate hazards infrared precipitation with stations – a new environmental record for monitoring extremes, Sci. Data, 2, 1–21, https://doi.org/10.1038/sdata.2015.66, 2015.

García-Alén, G., González-Cao, J., Fernández-Nóvoa, D., Gómez-Gesteira, M., Cea, L., and Puertas, J.: Analysis of two sources of variability of basin outflow hydrographs computed with the 2D shallow water model Iber: Digital Terrain Model and unstructured mesh size, J. Hydrol., 612, 128182, https://doi.org/10.1016/j.jhydrol.2022.128182, 2022.

García-Alén, G., Hostache, R., Cea, L., and Puertas, J.: Joint assimilation of satellite soil moisture and streamflow data for the hydrological application of a two-dimensional shallow water model, J. Hydrol., 621, 129667, https://doi.org/10.1016/j.jhydrol.2023.129667, 2023.

García-Feal, O., González-Cao, J., Gómez-Gesteira, M., Cea, L., Domínguez, J. M., and Formella, A.: An accelerated tool for flood modelling based on Iber, Water, 10, 1459, https://doi.org/10.3390/w10101459, 2018.

Garrote, J.: Free Global DEMs and Flood Modelling – A Comparison Analysis for the January 2015 Flooding Event in Mocuba City (Mozambique), Water, 14, 176, https://doi.org/10.3390/w14020176, 2022.

Gosset, M., Dibi-Anoh, P. A., Schumann, G., Hostache, R., Paris, A., Zahiri, E.-P., Kacou, M., and Gal, L.: Hydrometeorological extreme events in Africa: The role of satellite observations for monitoring pluvial and fluvial flood risk, Surv. Geophys., 44, 197–223, 2023.

Grimaldi, S., Li, Y., Pauwels, V., and Walker, J. P.: Remote sensing-derived water extent and level to constrain hydraulic flood forecasting models: Opportunities and challenges, Surv. Geophys., 37, 977–1034, https://doi.org/10.1007/s10712-016-9378-y, 2016.

Guth, P. L. and Geoffroy, T. M.: LiDAR point cloud and ICESat-2 evaluation of 1 second global digital elevation models: Copernicus wins, T. GIS, 25, 2245–2261, 2021.

Huffman, G. J., Bolvin, D. T., Braithwaite, D., Hsu, K.-L., Joyce, R. J., Kidd, C., Nelkin, E. J., Sorooshian, S., Stocker, E. F., Tan, J., Wolff, D. B., and Xie, P.: Integrated multi-satellite retrievals for the global precipitation measurement (GPM) mission (IMERG), In Satellite precipitation measurement Springer International Publishing, 343–353, https://doi.org/10.1007/978-3-030-24568-9_19, 2020.

Jaafar, H. and Ahmad, F.: GCN250, global curve number datasets for hydrologic modeling and design, figshare [data set], https://doi.org/10.6084/m9.figshare.7756202.v1, 2019.

Jaafar, H. H., Ahmad, F. A., and El Beyrouthy, N.: GCN250, New Global Gridded Curve Numbers for Hydrologic Modeling and Design, Sci. Data, 6, 145, https://doi.org/10.1038/s41597-019-0155-x, 2019.

Komi, K., Neal, J., Trigg, M. A., and Diekkrüger, B.: Modelling of flood hazard extent in data sparse areas: a case study of the Oti River basin, West Africa, J. Hydrol. Reg. Stud., 10, 122–132, https://doi.org/10.1016/j.ejrh.2017.03.001, 2017.

Kuntla, S. K. and Manjusree, P.: Development of an automated tool for delineation of flood footprints from sar imagery for rapid disaster response: a case study, J. Indian Soc. Remot., 48, 935–944, https://doi.org/10.1007/s12524-020-01125-4, 2020.

Krieger, G., Zink, M., Bachmann, M., Bräutigam, B., Schulze, D., Martone, M., Rizzoli, P., Steinbrecher, U., Walter Antony, J., De Zan, F., Hajnsek, I., Papathanassiou, K., Kugler, F., Rodriguez Cassola, M., Younis, M., Baumgartner, S., López-Dekker, P., Prats, P., and Moreira, A.: TanDEM-X: A radar interferometer with two formation-flying satellites, Acta Astronaut., 89, 83–98, 2013.

Lacamurima, F. M. M. R.: Impacto da precipitação nas cheias da Bacia do Umbelúzi, Trabalho de Licenciatura, Universidade Eduardo Mondlane, http://localhost:8080/xmlui/handle/123456789/422 (last access: 1 March 2023), 2003.

Liu, J., Du, J., Yang, Y., and Wang, Y.: Evaluating extreme precipitation estimations based on the GPM IMERG products over the Yangtze River Basin, China, Geomat. Nat. Haz. Risk, 11, 601–618, 2020.

Marešová, J., Gdulová, K., Pracná, P., Moravec, D., Gábor, L., Prošek, J., Barták, V., and Moudrý, V.: Applicability of Data Acquisition Characteristics to the Identification of Local Artefacts in Global Digital Elevation Models: Comparison of the Copernicus and TanDEM-X DEMs, Remote Sens., 13, 3931, https://doi.org/10.3390/rs13193931, 2021.

Moral-Erencia, J. D., Bohorquez, P., Jimenez-Ruiz, P. J., and Pérez-Latorre, F. J.: Flood hazard mapping with distributed hydrological simulations and remote-sensed slackwater sediments in ungauged basins, Water, 13, 3434, https://doi.org/10.3390/w13233434, 2021.

Morales-Hernández, M., Sharif, M. B., Kalyanapu, A., Ghafoor, S. K., Dullo, T., Gangrade, S., Kao, S., Norman, M. R., and Evans, K. J.: TRITON: A Multi-GPU Open Source 2D Hydrodynamic Flood Model, Environ. Model. Softw., 141, 105034, https://doi.org/10.1016/j.envsoft.2021.105034, 2021.

NASA: Atmospheric Composition, Water & Energy Cycles and Climate Variability, NASA [data set], https://disc.gsfc.nasa.gov (last access: 1 March 2023), 2023.

Nemni, E., Bullock, J., Belabbes, S., and Bromley, L.: Fully Convolutional Neural Network for Rapid Flood Segmentation in Synthetic Aperture Radar Imagery, Remote Sens., 12, 2532, https://doi.org/10.3390/rs12162532, 2020.

Noh, S. J., Lee, J. H., Lee, S., Kawaike, K., and Seo, D. J.: Hyper-resolution 1D-2D urban flood modelling using LiDAR data and hybrid parallelization, Environ. Model. Softw., 103, 131–145, 2018.

OCHA: Mozambique: Floods in Maputo city and province – Flash update No. 3 (as of 18 February 2023), Situation Report, https://reliefweb.int/report/mozambique/mozambique-floods-maputo-city-and-province-flash-update-no-3-18-february-2023 (last access: 1 March 2023), 2023.

Pradhan, R. K., Markonis, Y., Vargas Godoy, M. R., Villalba-Pradas, A., Andreadis, K. M., Nikolopoulos, E. I., Papalexiou, S. M., Rahim, A., Tapiador, F. J., and Hanel, M.: Review of GPM IMERG performance: A global perspective, Remote Sens. Environ., 268, 112754, https://doi.org/10.1016/J.RSE.2021.112754, 2022.

Revilla-Romero, B., Thielen, J., Salamon, P., De Groeve, T., and Brakenridge, G. R.: Evaluation of the satellite-based Global Flood Detection System for measuring river discharge: influence of local factors, Hydrol. Earth Syst. Sci., 18, 4467–4484, https://doi.org/10.5194/hess-18-4467-2014, 2014.

Ross, C. W., Prihodko, L., Anchang, J., Kumar, S., Ji, W., and Hanan, N. P.: HYSOGs250m, global gridded hydrologic soil groups for curve-number-based runoff modeling, Sci. Data, 5, 1–9, https://doi.org/10.1038/sdata.2018.91, 2018.

Sanders, B. F. and Schubert, J. E.: PRIMo: Parallel raster inundation model, Adv. Water Resour., 126, 79–95, 2019.

Sanz Ramos, M., Amengual, A., Bladé i Castellet, E., Romero, R., and Roux, H.: Flood forecasting using a coupled hydrological and hydraulic model (based on FVM) and highresolution meteorological model, in: E3S Web of Conferences, vol. 40, River Flow 2018-Ninth International Conference on Fluvial Hydraulics, 1–8, E3S Web of Conferences, 2018.

Sanz-Ramos, M., Bladé, E., González-Escalona, F., Olivares, G., and Aragón-Hernández, J. L.: Interpreting the Manning Roughness Coefficient in Overland Flow Simulations with Coupled Hydrological-Hydraulic Distributed Models, Water, 13, 3433, https://doi.org/10.3390/w13233433, 2021.

Sanz-Ramos, M., Cea, L., Bladé, E., López-Gómez, D., Sañudo, E., Corestein, G., García-Alén, G., and Aragón-Hernández, J. L.: Iber v3: manual de referencia e interfaz de usuario de las nuevas implementaciones, Universidade da Coruña, https://doi.org/10.23967/iber.2022.01, 2022.

Saouabe, T., El Khalki, E. M., Saidi, M. E. M., Najmi, A., Hadri, A., Rachidi, S., Jadoud, M., and Tramblay, Y.: Evaluation of the GPM-IMERG precipitation product for flood modeling in a semi-arid mountainous basin in Morocco, Water, 12, 2516, https://doi.org/10.3390/w12092516, 2020.

Sharifian, M. K., Kesserwani, G., Chowdhury, A. A., Neal, J., and Bates, P.: LISFLOOD-FP 8.1: new GPU-accelerated solvers for faster fluvial/pluvial flood simulations, Geosci. Model Dev., 16, 2391–2413, https://doi.org/10.5194/gmd-16-2391-2023, 2023.

Singh, V. P.: Handbook of applied hydrology, McGraw-Hill Education, ISBN 9780071835091, 2017.

Tamagnone, P., Cea, L., Comino, E., and Rosso, M.: Rainwater Harvesting Techniques to Face Water Scarcity in African's Drylands: Hydrological Efficiency Assessment, Water, 12, 2646, https://doi.org/10.3390/w12092646, 2020.

Tapiador, F. J., Marcos, C., Sancho, J. M., Santos, C., Núñez, J. Á., Navarro, A., Kummerow, C., and Adler, R. F.: The September 2019 floods in Spain: An example of the utility of satellite data for the analysis of extreme hydrometeorological events, Atmos. Res., 257, 105588, https://doi.org/10.1016/j.atmosres.2021.105588, 2021.

Uber, M., Nord, G., Legout, C., and Cea, L.: How do modeling choices and erosion zone locations impact the representation of connectivity and the dynamics of suspended sediments in a multi-source soil erosion model?, Earth Surf. Dynam., 9, 123–144, https://doi.org/10.5194/esurf-9-123-2021, 2021.

Universidade da Coruña and Universitat Politècnica de Catalunya CEDEX: Iber, Universidade da Coruña and Universitat Politècnica de Catalunya CEDEX [data set], http://www.iberaula.com (last access: 1 March 2023), 2024.

WMO: Reducing vulnerability to extreme hydro-meteorological hazards in Mozambique after Cyclone IDAI. WMO mission report following tropical cyclone IDAI (29 April to 7 May), World Meteorological Organization, Geneva, https://library.wmo.int/viewer/56658 (last access: 1 March 2023), 2019.

World Bank: Mozambique Disaster Risk Profile, World Bank, Washington, DC, https://documentos.bancomundial.org/es/publication/documents-reports/documentdetail/845611574234249644/disaster-risk-profile-mozambique (last access: 1 March 2023), 2019.

Xia, X., Liang, Q., and Ming, X.: A full-scale fluvial flood modelling framework based on a high-performance integrated hydrodynamic modelling system (HiPIMS), Adv. Water Resour., 132, 103392, https://doi.org/10.1016/j.advwatres.2019.103392, 2019.

Zhao, J., Pelich, R., Hostache, R., Matgen, P., Cao, S., Wagner, W., and Chini, M.: Deriving exclusion maps from C-band SAR time-series in support of floodwater mapping, Remote Sens. Environ., 265, 112668, https://doi.org/10.1016/j.rse.2021.112668, 2021.

Zink, M., Moreira, A., Hajnsek, I., Rizzoli, P., Bachmann, M., Kahle, R., Fritz, T., Huber, M., Krieger, G., Lachaise, M., Martone, M., Maurer, E., and Wessel, B.: TanDEM-X: 10 years of formation flying bistatic SAR interferometry, IEEE J. Sel. Top. Appl., 14, 3546–3565, 2021.

Zuhlke, M., Fomferra, N., Brockmann, C., Peters, M., Veci, L., Malik, J., and Regner, P.: SNAP (sentinel application platform) and the ESA sentinel 3 toolbox, In Sentinel-3 for Science Workshop, 734, 21 pp., https://ui.adsabs.harvard.edu/abs/2015ESASP.734E..21Z/abstract (last access: 1 March 2023), 2015.